20. J. E. Jackson and M. S. Platz, *Adv. Carbene Chem.* **1**, 89 (1994).
21. A. Admasu *et al.*, *J. Chem. Soc. Perkin Trans.* **2**, 1093 (1998).
22. 1,2-F migration leading to the corresponding alkene has been observed for transient singlet halogeno(trifluoromethyl)carbenes [J. E. O'Gara and W. P. Dailey, *J. Am. Chem. Soc.* **114**, 3581 (1992)]; moreover, C-fluorinated phosphorus ylides are known to rearrange into the corresponding phosphacumulene by 1,2-F migration from carbon to phosphorus [K. G. Sharp and I. Schwager, *Inorg. Chem.* **15**, 1697 (1976)].
23. R. T. Ruck and M. Jones Jr., *Tetrahedron Lett.* **39**, 2277 (1998).
24. The reaction of transient dihalogenocarbenes with phosphines is a preparative method for *C*-dihalogeno phosphorus ylides [H. J. Bestmann and R. Zimmermann, *Methoden der Organischen Chemie Organischen Chemie (Houben-Weyl)*, vol. E1 (Stuttgart, New York, 1982), pp. 616–618; A. W. Johnson *et al.*, in *Ylides and Imines of Phosphorus*, A. W. Johnson, Ed. (Wiley-Interscience, New York, 1993), pp. 115–116].
25. K. Krogh-Jespersen, S. Yan, R. A. Moss, *J. Am. Chem. Soc.* **121**, 6269 (1999).
26. R. A. Moss, S. Yan, K. Krogh-Jespersen, *J. Am. Chem. Soc.* **120**, 1088 (1998).
27. M. I. Khan and J. L. Goodman, *J. Am. Chem. Soc.* **117**, 6635 (1995).
28. For **6**, the trifluoromethyl group is anti to the original alkene substituent, as observed in the cycloaddition reaction of the MeO-C-CF_3 carbene with a similar alkene (*15*). In the latter case, steric interactions were postulated to be the cause of the observed high diastereoselectivity. Because the bis(dicyclohexylamino)phosphanyl group is rather more bulky than the CF_3 group, the stereoselectivity observed for **6** cannot be due to steric factors. In fact, for both carbenes (MeO-C-CF_3 and **3**), the results can be rationalized in terms of secondary orbital interaction control. See S. Goumri-Magnet, T. Kato, H. Gornitzka, A. Baceiredo, G. Bertrand, *J. Am. Chem. Soc.*, in press.
29. Various transient trifluoromethylcarbenes are known to insert into silicon-hydrogen bonds (*16*).
30. W. W. Schoeller, *Eur. J. Org. Chem.* **2**, 369 (2000).
31. Crystal data for **10** are available at *Science* Online (*33*).
32. Further evidence for the delocalization of the carbene lone pair includes the following (i) the short C1-C2 bond length (1.390 ± 0.004 Å), which indicates a double-bond character; (ii) the C2-C3 and C2-C7 bond distances, which are longer than the other bonds of the ring; and (iii) the ^{13}C NMR signals corresponding to C3, C5, and C7, which appear at high field, whereas those for C4 and C6 are more deshielded (*18*).
33. For supplementary data, see www.sciencemag.org/feature/data/1048933.shl.
34. We are grateful to the CNRS for financial support of this work.

27 January 2000; accepted 13 March 2000

Radar Observations of Asteroid 216 Kleopatra

Steven J. Ostro,[1]* R. Scott Hudson,[2] Michael C. Nolan,[3] Jean-Luc Margot,[3] Daniel J. Scheeres,[4] Donald B. Campbell,[5] Christopher Magri,[6] Jon D. Giorgini,[1] Donald K. Yeomans[1]

Radar observations of the main-belt, M-class asteroid 216 Kleopatra reveal a dumbbell-shaped object with overall dimensions of 217 kilometers by 94 kilometers by 81 kilometers (±25%). The asteroid's surface properties are consistent with a regolith having a metallic composition and a porosity comparable to that of lunar soil. Kleopatra's shape is probably the outcome of an exotic sequence of collisional events, and much of its interior may have an unconsolidated rubble-pile structure.

The main asteroid belt contains 42 objects whose optical spectra reveal the presence, but not the dominance, of NiFe metal. These M-class objects may include the parent bodies of some iron meteorites, which are thought to be derived from asteroids that melted, differentiated, and solidified within the first billion years of the solar system (*1*) and subsequently suffered collisional exposure of their metallic interiors. M-class asteroids have yet to be targeted for study by spacecraft, and detailed information about their physical properties is lacking. However, two decades of telescopic observations of the large M-class asteroid 216 Kleopatra have marked it as highly unusual. Optical light curves with large amplitudes (*2–4*) and stellar occultation timings (*5, 6*) suggest an elongated shape, and Doppler-only radar observations (*7*) and adaptive optics images (*8*) suggest some sort of shape bifurcation.

We used the S-band (2380 MHz, 12.6 cm) radar system of the recently upgraded Arecibo Observatory to obtain images on four dates in November 1999 (Table 1). Our observational and data-reduction techniques have been described by Harmon *et al.* (*9*). We transmitted a circularly polarized, nonrepeating, binary phase–coded waveform with a time resolution, or baud, equal to 0.1 ms (range resolution of 15 km) and sampled the echoes at intervals of 0.05 ms, in the same and opposite circular polarizations (SC and OC, respectively) simultaneously. Kleopatra's SC/OC radar cross-section ratio is 0.00 ± 0.05 (*7*), and our analyses used only the OC data.

Each run produced a 41 by 41 pixel delay-Doppler image (Fig. 1). Delay bins are 0.05 ms (7.5 km) deep, but because the echoes were double sampled, there is correlation between adjacent delay bins; our analysis took this correlation into account. For a rotating rigid object with Kleopatra's optically determined spin period (5.385 hours) (*10*), the distance equivalent of our frequency resolution, 19.5 Hz (chosen to optimize the tradeoff between pixel size and signal-to-noise ratio), is 3.8 km/cos δ, where δ is the subradar latitude. All data were taken with Kleopatra within 1.8° of the apparent right ascension, 61.4°, and declination, 11.8°. Our estimated pole direction (ecliptic longitude, 72°; latitude, 27°), 8° from the pole direction (71°, 19°) estimated from optical light curves (*10*), corresponds to δ = −53° and a frequency-pixel resolution of 6.3 km.

The asteroid's delay-Doppler signature is bimodal. In the most end-on images, which show the maximum echo-delay depth and minimum bandwidth, the leading edges of the two lobes are ~60 km apart. However, our view was several tens of degrees from pole on, and the actual distance between those edges is ~100 km. The peak echo power in any of our raw, unsmoothed images (Fig. 1) is 9 standard deviations. With such modest echo strength, the absence of echo at delays between the two lobes does not necessarily mean that the space between the two lobes is empty, but rather that there is relatively little normally oriented surface area facing the radar in those pixels. The stronger images taken in broadside orientations, which show the maximum bandwidth and minimum delay depth, do show significant echoes from the part of the asteroid between the two lobes. (Echoes from surface elements that contain the plane-of-sky projection of the asteroid's spin vector have levels of 2 to 4 standard deviations at the images' raw resolution and higher if smoothed.) Thus, the interlobe surface reflects detectable echoes only in certain orientations (Figs. 1 and 2).

We used least squares inversion (*11–15*) to estimate Kleopatra's shape (256 parameters), radar-scattering law (2 parameters), and pole direction (2 parameters) (Figs. 2 and 3). We adopted Kleopatra's optically derived spin period (*10*) and assumed principal axis rotation and uniform density. There is correlation between the object's size, its angular-scattering law, and cos δ; we adjusted the pole direction to force the scale of the model to be consistent with the scale of the stellar occultation chords reported by Dunham (*5, 6*).

[1]Jet Propulsion Laboratory, California Institute of Technology, Pasadena, CA 91109–8099, USA. [2]School of Electrical Engineering and Computer Science, Washington State University, Pullman, WA 99164–2752, USA. [3]Arecibo Observatory, HC3 Box 53995, Arecibo, PR 00612, USA. [4]Department of Aerospace Engineering, University of Michigan, Ann Arbor, MI 48109–2140, USA. [5]Department of Astronomy, Space Sciences Building, Cornell University, Ithaca, NY 14853, USA. [6]University of Maine at Farmington, Preble Hall, 39 High Street, Farmington, ME 04938, USA.

*To whom correspondence should be addressed. E-mail: ostro@reason.jpl.nasa.gov

The asteroid is shaped like a dumbbell with a handle that looks substantially narrower than the two lobes when seen pole on but not when seen from within the equatorial plane (Fig. 3). Our model's dimensions as defined by its extents parallel to the principal axes are 217 km by 94 km by 81 km (Fig. 3). The dynamically equivalent equal-volume ellipsoid, that is, the homogeneous ellipsoid that has the same moment-of-inertia ratios (1:7.03:7.08) and the same volume (67×10^4 km^3) as the shape model, has dimensions of 257 km by 72 km by 69 km. The uncertainty in the model's shape (Figs. 2 and 3) is ~15 km; additionally, the uncertainty in the model's absolute size is as large as 25%.

The asteroid's low SC/OC ratio indicates that nearly all of the echo is due to single back-reflections from facets that are oriented nearly normal to the radar line of sight and are smooth at decimeter scales. If Kleopatra's handle were cylindrical (or were defined by translation along its axis of any closed curve), it would present no normally oriented area except in the broadside (maximum-bandwidth) orientation. The quasi-cylindrical character of Kleopatra's handle explains why it returns so little echo in most of our radar images.

In the shape reconstruction, we assumed Kleopatra's radar properties to be uniform and adjusted the two parameters ρ and n in a simple backscattering law, $d\sigma/dA = \rho \cos^n \theta$, where σ is radar cross section and A is surface area. If a Parker probability density function is assumed to describe the distribution of surface slopes with respect to the model shape, then our estimation yields the Fresnel power reflection coefficient $R = 2\rho/(n + 2)$ and the adirectional root-mean-square slope $S_{rms} = \tan^{-1}[(2/n)^{1/2}]$ of unresolved facets relative to the reconstructed shape (*7*). We obtained $n = 4.0 \pm 1.5$, $S_{rms} = 35° \pm 4°$, and $R = 0.50$. Our estimate of S_{rms} is comparable to corresponding values for other main-belt asteroids (*16*) but about five times as large as lunar values (*17*). Kleopatra's average radar albedo (that is, radar cross section per unit of projected surface area) is 0.7. A sphere with Kleopatra's scattering parameters would have a radar albedo of 0.6. R and those albedos are uncertain to ~50% because of uncertainties in the shape model and in the absolute calibration of the radar images. Kleopatra is the most reflective of the several dozen radar-detected main-belt asteroids (*18*) and is about an order of magnitude more reflective than the moon. Its reflectivity is comparable to that of the several-kilometer object 6178 (1986 DA), which is the most reflective of the several dozen radar-detected near-Earth asteroids (*19*).

M-class meteorite analogs are irons, which are NiFe metal, and enstatite chondrites, which are assemblages of NiFe metal and enstatite. All enstatite chondrites may be derived from a single parent body, whereas the sample of iron meteorites may be derived from at least a dozen parent bodies. Combining information about the composition and density of those meteorite types with theoretical and empirical understanding of the electrical properties of metal-containing rocks and powders (*19*), we find that our reflectivity estimates imply a surface bulk density of no less than 3.5 g cm^{-3}, consistent with either a solid enstatite-chondritic surface or a metallic surface with porosity of <60%. Nearly all estimates of the porosity of lunar soil fall between 35 and 55% (*20*).

The physical properties of Kleopatra's surface are constrained by calculation (*21*) of the global distribution of escape speed (V_{esc}) and gravitational slope (S_{grav}, the angle be-

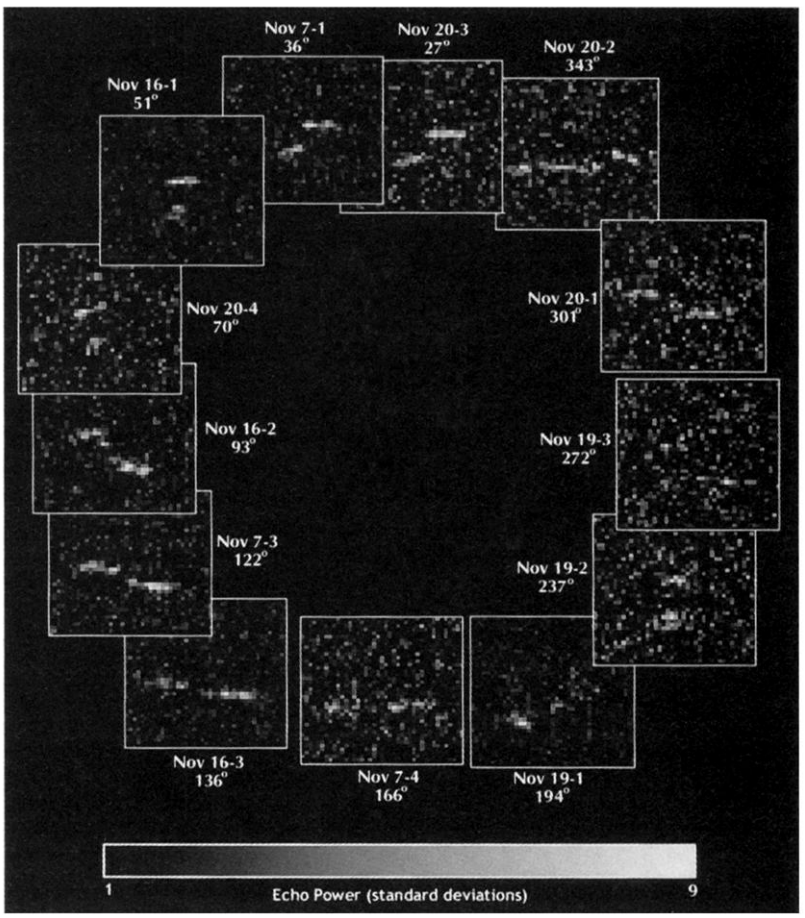

Fig. 1. Radar images organized by relative rotation phase (Table 1). Time delay (range) increases toward the bottom and Doppler frequency increases toward the right; therefore, the asteroid's rotation is counterclockwise.

Table 1. Observations from November 1999. UTC RCV is the reception interval and UTC mid is the reception midpoint. TPWR is transmitter power, RTT is echo round-trip time delay, and σ is the OC radar cross section.

Day	Run	UTC RCV		UTC mid	Interval time (s)	TPWR (kW)	RTT (s)	Relative rotation phase	σ (km^2)
		Start	Stop						
7	1	0445:51	0457:50	0452	719	475	1150.3	36°	6,100
7	3	0559:47	0618:50	0609	1143	412	1150.2	122°	11,000
7	4	0638:17	0657:20	0648	1143	412	1150.1	165°	8,500
16	1	0420:08	0439:00	0429	1132	456	1139.8	51°	9,000
16	2	0458:08	0517:00	0507	1132	448	1139.8	93°	5,900
16	3	0536:08	0555:00	0545	1132	453	1139.8	136°	4,100
19	1	0428:29	0447:22	0438	1133	456	1140.9	194°	8,000
19	2	0506:31	0525:24	0516	1133	450	1140.9	237°	1,200
19	3	0544:33	0552:29	0548	476	457	1140.9	272°	470
20	1	0337:09	0356:03	0346	1134	456	1141.7	301°	9,900
20	2	0415:13	0434:07	0424	1134	449	1141.7	343°	9,100
20	3	0453:17	0512:11	0503	1134	444	1141.7	27°	7,000
20	4	0531:21	0550:15	0542	1134	452	1141.8	70°	7,500

tween a plumb line and the local surface normal). Taking into account uncertainties in our model's size and shape, we find that, for a uniform internal density $d = 3.5$ g cm^{-3}, the distribution of V_{esc} has a minimum of at least 40 m s^{-1} and a maximum of at least 138 m s^{-1}, averaging at least 76 m s^{-1}; corresponding values for $d = 7.5$ g cm^{-3} are 73, 202, and 113 m s^{-1}, respectively. These relatively high speeds imply that a large proportion of impact-cratering ejecta have returned to the surface. S_{grav}, whose density dependence here is negligible, averages 15° ± 3°, almost nowhere exceeds 30°, and never exceeds 40°. For terrestrial slopes composed of mixtures of particle sizes, the angle of repose is usually between 34° and 37° (*22*). Whereas some of Kleopatra's largest values of S_{grav} may be due to large outcrops of rigid solid material, the predominantly gentle slopes and the low SC/OC ratio indicate a surface that is almost completely covered by "relaxed" regolith whose particles are in stable, low-potential-energy locations. This result is consistent with the expectation (*23*) that meteoroid bombardment of asteroids as large as Kleopatra has produced regoliths ten to several hundred meters deep. The evidence for a porous regolith and a high surface bulk density rules out an enstatite-chondritic composition.

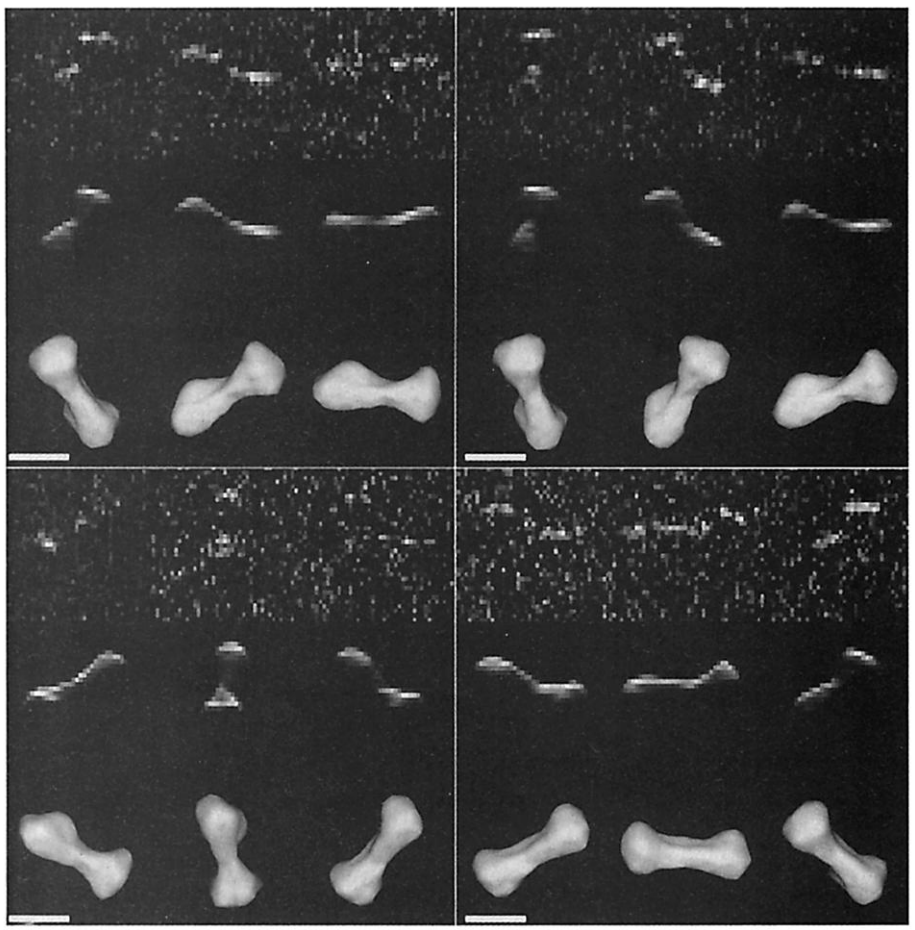

Fig. 2. Shape reconstruction results. Each quadrant shows Arecibo radar images from one date (top), corresponding images calculated from the shape model (middle), and corresponding plane-of sky views of the model (bottom). The top left, top right, bottom left, and bottom right quadrants correspond to 7, 16, 19, and 20 November, respectively, with columns arranged chronologically within each quadrant (Table 1) (the last run on 20 November was omitted). Each scale bar represents 100 km. In the radar images, time delay increases toward the bottom and Doppler frequency increases toward the right. In the plane-of-sky views, north is up.

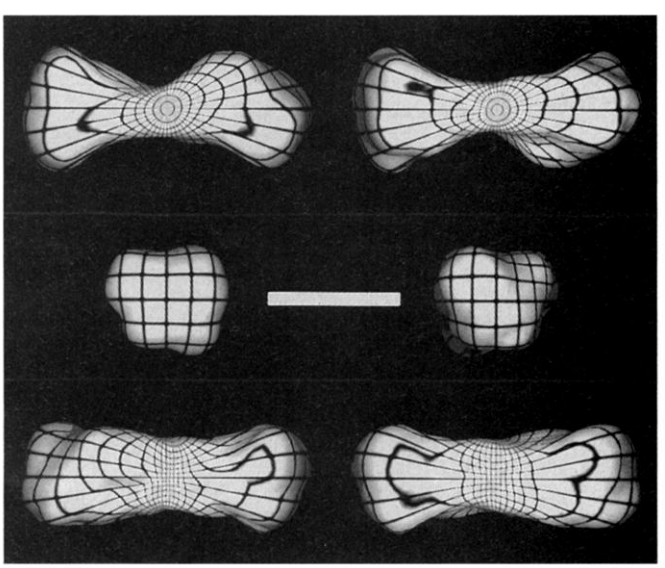

Fig. 3. Views of the Kleopatra shape model parallel to its principal axes of inertia. The scale bar represents 100 km. Contours of longitude and latitude are spaced by 10°. The spin vector (the north pole) points toward the reader in the top left frame.

Kleopatra's bifurcation suggests that its lobes once were two separate entities (*24*). Its dumbbell shape may have resulted from a gentle collision between two objects, from low-velocity infall of adjacent fragments after a disruption event, or from tidal decay of a binary system formed temporarily by a disruption (*25, 26*). Simulated collisions (*27*) of rubble-pile asteroids (*28, 29*) have produced bifurcated shapes; perhaps the disruption of Kleopatra's parent core created two fragmented objects that later collided to form a dumbbell-shaped body.

Each of these scenarios suggests that much of Kleopatra's interior might be relatively unconsolidated debris, perhaps including some number of large monolithic shards. Compared to a purely monolithic structure, such a configuration would more easily survive impact bombardment over billion-year time scales (*30, 31*). Moreover, impact sculpturing of a monolithic dumbbell would require rather contrived geometrical circumstances, and it seems unlikely that Kleopatra's regolith might conceal either its parent body's original intact core or a single, highly elongated piece of it. Still, given the current level of understanding of how asteroids differentiated and collisionally evolved, we are reluctant to rule out even the more exotic possibilities. Computer simulation of catastrophic and multigenerational, subcatastrophic collisions using equations of state for metal might lead to a convincing model for Kleopatra's formation.

References and Notes

1. E. R. D. Scott *et al.*, in *Asteroids II*, R. P. Binzel, T. Gehrels, M. S. Matthews, Eds. (Univ. of Arizona Press, Tucson, 1989), pp. 701–739.
2. F. Scaltriti and V. Zappalà, *Icarus* **34**, 428 (1978).

3. D. J. Tholen, *Sky Telescope* **60**, 203 (1980).
4. V. Zappalà, M. Di Martino, F. Scaltriti, G. Djurašević, Z. Knežević, *Icarus* **53**, 458 (1983).
5. D. W. Dunham, *Occultation Newsl.* **2**, 139 (1981).
6. ———, *Sky Telescope* **83**, 73 (1992).
7. D. L. Mitchell *et al.*, *Icarus* **118**, 105 (1995).
8. F. Marchis, D. Hestroffer, A. Cellino, P. Tanga, V. Zappalà, *IAU Circ. 7308* (Smithsonian Astrophysical Observatory, Cambridge, MA, 1999).
9. J. K. Harmon, R. E. Arvidson, E. A. Guinness, B. A. Campbell, M. A. Slade, *J. Geophys. Res.* **104**, 14065 (1999).
10. P. Magnusson *et al.*, *Icarus* **85**, 229 (1990).
11. R. S. Hudson and S. J. Ostro, *Science* **263**, 940 (1994).
12. ———, *Science* **270**, 84 (1995).
13. The accuracy of our inversion technique has been calibrated with extensive Monte Carlo simulations and laboratory laser-radar experiments (*14*).
14. A. K. Andrews, R. S. Hudson, D. Psaltis, *Opt. Lett.* **20**, 2327 (1995).
15. Inversions with disparate initial conditions (including an ellipsoid and, to test the possibility that a binary system might explain the images, two co-orbiting spheres) each yielded a dumbbell shape.
16. D. L. Mitchell *et al.*, *Icarus* **124**, 113 (1996).
17. R. A. Simpson and G. L. Tyler, *IEEE Trans. Antennas Propag.* **AP-30**, 438 (1982).
18. C. Magri *et al.*, *Icarus* **140**, 379 (1999).
19. S. J. Ostro *et al.*, *Science* **252**, 1399 (1991).
20. W. D. Carrier III, J. K. Mitchell, A. Mahmood, *Proc. Lunar Sci. Conf.* **4**, 2403 (1973).
21. D. J. Scheeres, S. J. Ostro, R. S. Hudson, E. M. DeJong, S. Suzuki, *Icarus* **132**, 53 (1998).
22. A. N. Strahler, *The Earth Sciences* (Harper & Row, New York, ed. 3, 1971).
23. D. S. McKay, T. D. Swindle, R. Greenberg, in *Asteroids II*, R. P. Binzel, T. Gehrels, M. S. Matthews, Eds. (Univ. of Arizona Press, Tucson, 1989), pp. 617–642.
24. Our data and model alone do not rule out the presence of an empty gap, up to a few kilometers wide, in the middle of the asteroid. However, such a gap would require our model's internal density to be <3.4 g cm^{-3}, below our lower limit on the asteroid's surface bulk density.
25. W. K. Hartmann and D. P. Cruikshank, *Icarus* **36**, 353 (1978).
26. W. K. Hartmann, in *Asteroids*, T. Gehrels, Ed. (Univ. of Arizona Press, Tucson, 1979), pp. 466–479.
27. Z. M. Leinhardt, D. C. Richardson, T. Quinn, *Icarus*, in press.
28. D. R. Davis, C. R. Chapman, R. Greenberg, S. J. Weidenschilling, A. W. Harris, in *Asteroids*, T. Gehrels, Ed. (Univ. of Arizona Press, Tucson, 1979), pp. 528–557.
29. P. Farinella, P. Paolicchi, V. Zappalà, *Icarus* **52**, 409 (1982).
30. E. Asphaug, S. J. Ostro, R. S. Hudson, D. J. Scheeres, W. Benz, *Nature* **393**, 437 (1998).
31. C. R. Chapman, W. J. Merline, P. Thomas, *Icarus* **140**, 28 (1999).
32. Part of this research was conducted at the Jet Propulsion Laboratory, operated by the California Institute of Technology under contract with NASA. The Arecibo Observatory is part of the National Astronomy and Ionosphere Center, which is operated by Cornell University under a cooperative agreement with NSF with support from NASA. R.S.H. was partially supported by NASA grant NAGW-4636. D.J.S. was partially supported by NASA grant NAGW-9017. D.B.C. was partially supported by NASA grant NAG 5-4220. C.M. was partially supported by NSF grant AST-9973216. We are grateful to A. Crespo, P. Perillat, S. Suzuki, A. Hine, J. K. Harmon, E. M. DeJong and the staff of the Arecibo Observatory.

10 February 2000; accepted 27 March 2000

Large-Scale Thermal Events in the Solar Nebula: Evidence from Fe,Ni Metal Grains in Primitive Meteorites

Anders Meibom,[1]*† Steven J. Desch,[2] Alexander N. Krot,[1] Jeffrey N. Cuzzi,[2] Michael I. Petaev,[3] Lionel Wilson,[4] Klaus Keil[1,5]

Chemical zoning patterns in some iron, nickel metal grains from CH carbonaceous chondrites imply formation at temperatures from 1370 to 1270 kelvin by condensation from a solar nebular gas cooling at a rate of ~0.2 kelvin per hour. This cooling rate requires a large-scale thermal event in the nebula, in contrast to the localized, transient heating events inferred for chondrule formation. In our model, mass accretion through the protoplanetary disk caused large-scale evaporation of precursor dust near its midplane inside of a few astronomical units. Gas convectively moved from the midplane to cooler regions above it, and the metal grains condensed in these parcels of rising gas.

Chondrules and Ca,Al-rich inclusions (CAIs) in primitive meteorites (chondrites) offer insights into events that took place in the solar nebula during the earliest stages of planetary formation ~4.56 billion years ago. Chondrules are millimeter-sized silicate spherules that formed by melting of solids during localized, transient, and repetitive heating events with peak temperatures in the range of 1800 to 2100 K [e.g., (*1*)]. Dynamic crystallization experiments reproduce chondrule textures similar to those of the most abundant porphyritic chondrules only when the cooling rate is ~100 to 1000 K hour^{-1} (*2*, *3*). The CAIs consist of refractory silicate and oxide minerals that are inferred to condense out of a cooling gas of solar composition [e.g., (*4*)]. However, most CAIs have experienced subsequent thermal processing resulting in melting and evaporation [e.g., (*5*)]. Comparison with dynamic crystallization experiments constrains the cooling rates of CAIs that crystallized from melts (type B) to 2 to 50 K hour^{-1} at temperatures around 1700 to 1800 K (*6*). In this way, chondrules and CAIs offer important constraints on the thermal evolution of the solar nebula during processing of preexisting solids. However, constraints on the thermal evolution of the nebula gas during formation of the first solids by gas-solid condensation are lacking.

Recently, Fe,Ni metal grains with chemical zoning patterns in Fe, Ni, Co, and Cr resulting from gas-solid condensation (*7*–*12*) were described in CH, CR, and Bencubbin-like chondrites (*13*–*15*). Some metal grains in CH chondrites, amounting to a fraction (10^{-4} to 10^{-2}) of all metal grains, appear to have condensed from a gas of solar composition at a total gas pressure of ~10^{-4} bar at temperatures from 1370 to 1270 K (*13*). During this process, the metal grains must have grown sufficiently fast and the gas must have cooled sufficiently fast to avoid homogenization of the zoned patterns by solid-state diffusion. Here we estimate the growth rate of the zoned metal grains, obtain a cooling rate for the region of the nebula from which they condensed, and discuss a possible astrophysical setting of this event.

We model gas-solid condensation of metal grains from a cooling gas of solar composition at a total pressure of 10^{-4} bar. For simplicity, we assume that the growing metal grains are spherical in shape and consist of Fe atoms [zoned metal grains contain <10 weight % (wt %) Ni, Co, and Cr] and that the metal grains grow by Fe atoms continuously colliding with and sticking to the surface of the growing grain with a sticking coefficient of 1 (*16*, *17*). The number of hits of Fe atoms per second on a sphere of radius a is $Z = \pi a^2 n_g(\mathrm{Fe}) V_{avg}(\mathrm{Fe})$, where $n_g(\mathrm{Fe})$ is the number density of Fe atoms in the gas and $V_{avg}(\mathrm{Fe}) = (8kT/\pi m_{Fe})^{1/2}$ is the mean speed of Fe atoms in the gas (Maxwell distribution) [where k is the Boltzmann constant, T is the temperature (in K), and m_{Fe} is the atomic weight of the Fe atom]. The number density of Fe atoms in solid Fe metal is $n_s(\mathrm{Fe})$, and the growth rate of the sphere is $n_s(\mathrm{Fe}) 4\pi a^2 da = Z dt \Rightarrow da/dt = n_g(\mathrm{Fe}) V_{avg}(\mathrm{Fe})/4n_s(\mathrm{Fe})$, where t is time. In gas of solar composition (*18*) at 1320 K and 10^{-4} bar, $n_g(\mathrm{Fe}) = 3 \times 10^{16}$ m^{-3} and $V_{avg}(\mathrm{Fe}) = 705$ m s^{-1}. The

[1]Hawai'i Institute of Geophysics and Planetology, School of Ocean and Earth Science and Technology, University of Hawai'i at Manoa, Honolulu, HI 96822, USA. [2]NASA Ames Research Center, Mail Stop 245-3, Moffett Field, CA 94035, USA. [3]Harvard-Smithsonian Center for Astrophysics, 60 Garden Street, Mail Stop 52, Cambridge, MA 02138, USA. [4]Environmental Science Department, Institute of Environmental and Natural Sciences, Lancaster University, Lancaster LA1 4YQ, UK. [5]Hawai'i Center for Volcanology, University of Hawai'i at Manoa, Honolulu, HI 96822, USA.

*To whom correspondence should be addressed. E-mail: meibom@pangea.stanford.edu
†Present address: Department of Geological and Environmental Sciences, Stanford University, Building 320, Lomita Mall, Stanford, CA 94305-2115, USA.